*Biopolymer Applications Journal* **Youcef MEHIR et al. Vol 5. N°1, 2026, pp. 39-51**
*e-ISSN : 2800-1729*

# Orthotropic Elastic Characterization of FDM PLA via Multi-axial Mechanical Testing

Youcef MEHIR [1*]; Abdelkader BENAOUALI [1]; Yacine BENABID [1]; Adel BELATTAR [1]; Ahmed SALMI [1]; Iskander Med Aimen BELHOUT [1]

*1: Mechanical Systems Design Laboratory, Ecole Militaire Polytechnique, Algiers, Algeria*
*Corresponding author*: mehir.youcef.emp@gmail.com*
Received: 4 November 2025; Accepted: 19 December 2025; Published: 18 January 2026;

**Abstract**

***This study investigates the orthotropic elastic behavior of Polylactic Acid (PLA) manufactured using Fused Deposition Modeling (FDM). According to ISO 527-2 and ASTM standards, standardized tensile and shear specimens were printed along the X, Y, and Z axes. A Box–Behnken Design of Experiments (DoE) was employed to investigate the influence of three key process parameters on the mechanical response: layer thickness, raster width, and printing speed. Directional Young's moduli (Ex, Ey, Ez) and shear moduli (Gxy, Gyz, Gzx) were obtained through mechanical testing. The results revealed a pronounced anisotropy induced by the layer-by-layer deposition process. We used the experimental data to make the full elastic stiffness matrix for the PLA, which is an orthotropic material. Statistical analysis (ANOVA) confirmed that process parameters had the biggest effect on changes in stiffness. The results give us a lot of information that we can use to model printed PLA parts in finite element simulations and help us come up with better ways to design 3D printed parts that work well mechanically.***

***Keywords:*** *Additive Manufacturing, Anisotropy, Design of Experiments, FDM, Polylactic Acid.*

## I. Introduction

Additive manufacturing (AM) has emerged as one of the most transformative manufacturing technologies of the past two decades. It is used in the aerospace, automotive, and biomedical fields[1]. In contrast to traditional subtractive methods, which take material away from a solid block, AM makes parts by adding material layer by layer. This method makes it feasible to make very complicated shapes that are hard or even impossible to make with machining, casting, or other standard manufacturing methods. Fused Deposition Modeling (FDM) is the most popular of the different AM technologies, such as Stereolithography (SLA) and Selective Laser Sintering (SLS). This popularity is attributed to its cost-effectiveness, process flexibility, ease of implementation, and compatibility with a wide range of thermoplastic polymers [2]. The layer-by-layer deposition method, However, the layer-by-layer deposition process inherently induces anisotropic mechanical, which means that the mechanical characteristics change depending on how the object is oriented [3].

The increasing use of AM has also changed how designs are made, especially by adding topology optimization (TO) to the design-for-additive-manufacturing (DfAM) technique [4]. TO's goal is to create structures that are both lightweight and mechanically efficient by spreading out the material in the best way possible within a particular design space. In this regard, numerous studies have underscored the significance of considering the anisotropic behavior of additive manufacturing (AM) materials during TO. Xu et al[5] illustrated the advantages of hybrid deposition strategies in enhancing the strength of FDM-manufactured structures, whereas Zou and Xia[6] underscored the necessity of incorporating anisotropic strength constraints to more accurately represent the actual performance of printed components. In the same way, Zhou et al [7] added the effects of build orientation to multi-component TO frameworks, which made AM constructions more mechanically reliable. These advancements exemplify the convergence of AM and TO, since AM's ability to produce intricate geometries inherently complements the advanced designs created by TO [8, 9].

In addition to design factors, the mechanical properties of FDM products are quite sensitive to process parameters such as layer thickness, raster width, and printing speed. Changes in these factors have a direct effect on the final product's stiffness, strength, and level of anisotropy. This dependence has spurred significant research initiatives aimed at quantifying and modeling the relationship between printing conditions and material properties [10-12]. Establishing predictive correlations is particularly advantageous since it allows designers to foresee the performance of printed structures and adjust process settings accordingly. In this respect, the current study examines the elastic orthotropy of FDM-manufactured PLA, aiming to deliver a comprehensive characterization of its mechanical behavior under varying

loading situations. The goal is to improve the accuracy and reliability of FDM materials by combining experimental testing and modeling methods. This will help create predictive models that are specific to DfAM applications.

## II. General Methodology

### 1) Orthotropy hypothesis: modeling filament orientation

Parts manufactured by FDM exhibit intrinsically anisotropic mechanical behavior, resulting from the layered nature of the process and the inherent directionality of the material deposition. To accurately capture this behavior, an orthotropic material assumption is commonly adopted, assuming the existence of three orthogonal planes of material symmetry associated with distinct mechanical properties[13,14].

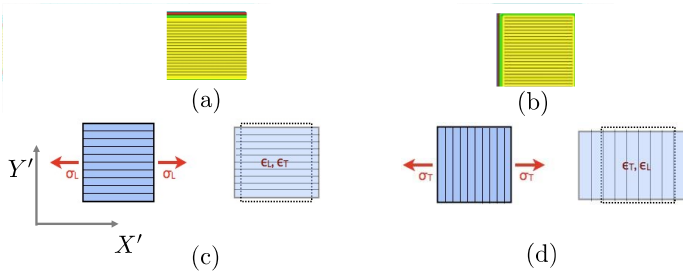


*Figure 1 Analogy underlying the orthotropic material assumption: (a) and (b) FDM printing along X' and Y' directions, respectively;*

Figure 1 illustrates this analogy by comparing RDs with their equivalent fiber-reinforced composite representations: subfigures Figure 1(a)–(b) show printing along the longitudinal \(X'\) and transverse \(Y'\) directions, while subfigures Figure 1(c)–(d) depict the corresponding composite systems with fibers aligned parallel or perpendicular to \(X'\). This observation confirms that the raster direction (RD) governs the principal axes of orthotropy in FDM-manufactured materials.

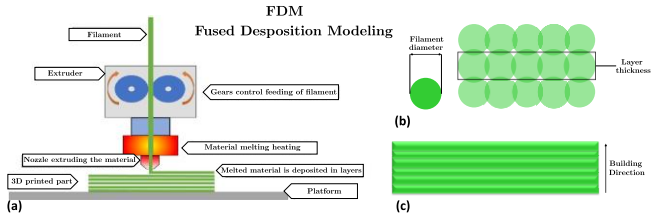


*Figure 2(a) FDM process (b) Filament arrangement (c) Layered structure*

Accordingly, the material is characterized by three principal directions: the **longitudinal direction** *X'*, aligned with RD and providing the highest stiffness; the **transverse in-plane direction** *Y'*, lying within the layer plane and perpendicular to *X'*; and the **build direction** *Z'* (see **Erreur ! Source du renvoi introuvable.**(c)), normal to the layers and mainly governed by interlayer bonding.

**Erreur ! Source du renvoi introuvable.** further illustrates the layer-by-layer deposition along Z', where the extruded filament acts as an oriented fiber. This layered architecture produces the anisotropic behavior of FDM components, as confirmed by the microstructures shown in subfigures **Erreur ! Source du renvoi introuvable.**(b)–(c).

Building upon this characterization, the proposed TO formulation incorporates the PSP relationships through a orthotropic model linking the mechanical properties to the RD and the printing parameters.

### 2) The element stiffness matrix $K_e(\theta, \alpha, \chi)$

The integration of the 3D orientations of the filaments $(\theta_e, \alpha_e)$ and the process parameters $(\chi)$ as design variables has a direct impact on the element stiffness matrix $K_e$.

$$K_e = \int_{\Omega_e} B_e^T D_e(\theta_e, \alpha_e, \chi)\, B_e d\Omega_e \qquad (1)$$

The integral presented in Equation (1) is generally not analytically solvable, especially for elements with complex shapes or when the terms of the integrand $(B_e \text{or } D_e)$ vary within the element.

Therefore, numerical integration methods are used, the most common in Finite Element Method being the Gauss–Legendre quadrature.

This method approximates the integral by a weighted sum of the values of the integrand evaluated at specific points, called Gauss points $(\xi_i, \eta_i, \zeta_i)$ in the natural coordinate system of the element, and associated with weights $W_i, W_j, W_k$.

$$\begin{aligned} K_e = \\ \sum_{p=1}^{n_{gp}} \sum_{q=1}^{n_{gp}} \sum_{r=1}^{n_{gp}} W_p W_q W_r \cdot \\ B_e(\xi_p, \eta_q, \zeta_r)^T \cdot \\ D_e(\theta_e, \alpha_e, \chi) \cdot \\ B_e(\xi_p, \eta_q, \zeta_r) \cdot \\ \det\left(J(\xi_p, \eta_q, \zeta_r)\right) \end{aligned} \qquad (2)$$

where $n_{gp}$ is the number of Gauss points in each direction of the natural coordinate system, and represents the application of this quadrature.

The term $\det\left(J(\xi_p, \eta_q, \zeta_r)\right)$ is the determinant of the Jacobian matrix of the transformation between global and natural coordinates, evaluated at the Gauss point, which appears in the change of variables $d\Omega_e = \det(J) \mathrm{d}\xi d\eta d\zeta$. Gauss–Legendre quadrature offers high numerical accuracy while requiring a limited number of integration points, by exactly integrating polynomials up to a certain degree. For example, an $n_{gp}$ point rule exactly integrates a polynomial of degree $2n_{gp} - 1$. The

Gauss points and weights are optimally chosen to achieve this accuracy[15].

### a) Orthotropic Material Elasticity Law

With the introduction of a three-dimensional orientation, the full orthotropic model, characterized by three mutually orthogonal planes of material symmetry, is more appropriate to describe the behavior of FDM parts, where the properties may differ significantly along the extrusion direction, the transverse direction in the deposition plane, and the direction perpendicular to the deposition plane (build direction)[15].

- **2D case:**
  For an orthotropic material under plane stresses, the elasticity matrix is given by:

$$D_{2D} = \begin{bmatrix} \frac{1}{E_{X'}} & \frac{-\nu_{X'Y'}}{E_{X'}} & 0 \\ \frac{-\nu_{X'Y'}}{E_{X'}} & \frac{1}{E_{Y'}} & 0 \\ 0 & 0 & \frac{1}{G_{X'Y'}} \end{bmatrix} \quad (3)$$

where $E_{X'}$ and $E_{Y'}$ are the Young's moduli in the principal directions, $\nu_{X'Y'}$ is the principal Poisson's ratio, and $G_{X'Y'}$ is the shear modulus in the plane.

- **3D case:**
  In 3D, the complete orthotropic elasticity matrix is:

$$D_{3D} = \begin{bmatrix} \frac{1}{E_{X'}} & & & & & \\ \frac{-\nu_{X'Y'}}{E_{X'}} & \frac{1}{E_{Y'}} & & & sym & \\ \frac{-\nu_{X'Z'}}{E_{X'}} & \frac{-\nu_{Y'Z'}}{E_{X'}} & \frac{1}{E_{Z'}} & & & \\ & & & \frac{1}{G_{Y'Z'}} & & \\ & 0 & & & \frac{1}{G_{X'Z'}} & \\ & & & & & \frac{1}{G_{X'Y'}} \end{bmatrix} \quad (4)$$

  There are nine independent coefficients: Young's three moduli, Poisson's three coefficients, and the three shear moduli. It is therefore easy to verify that the orthotropic model.

Accurately modeling these dependencies lies at the core of the PSP $(\chi)$ relationships $E_i(\chi), G_{ij}(\chi)$.

### b) Transformation matrices

- **Transformation for rotation around the z-axis (angle $\theta$)}**

The transformation matrix for a rotation of angle $\boldsymbol{\theta}$ around the $\boldsymbol{Z'}$ axis is:

$$T_\theta = \begin{bmatrix} (\cos\theta)^2 & (\sin\theta)^2 & 0 & 0 & 0 & -2\cos\theta\sin\theta \\ (\sin\theta)^2 & (\cos\theta)^2 & 0 & 0 & 0 & 2\cos\theta\sin\theta \\ 0 & 0 & 1 & 0 & 0 & 0 \\ 0 & 0 & 0 & \cos\theta & \sin\theta & 0 \\ 0 & 0 & 0 & -\sin\theta & \cos\theta & 0 \\ \cos\theta\sin\theta & -\cos\theta\sin\theta & 0 & 0 & 0 & cos^2\theta - sin^2\theta \end{bmatrix} \quad (5)$$

- **Transformation for rotation around the $X'Y'$ plane (angle $\alpha$)**

Similarly, for a rotation of angle $\boldsymbol{\alpha}$ around the $X'$ axis:

$$T_\alpha = \begin{bmatrix} 1 & 0 & 0 & 0 & 0 & 0 \\ 0 & (\cos\alpha)^2 & (\sin\alpha)^2 & -2\cos\alpha\sin\alpha & 0 & 0 \\ 0 & (\sin\alpha)^2 & (\cos\alpha)^2 & 2\cos\alpha\sin\alpha & 0 & 0 \\ 0 & \cos\alpha\sin\alpha & -\cos\alpha\sin\alpha & (\cos\alpha)^2 - (\sin\alpha)^2 & 0 & 0 \\ 0 & 0 & 0 & 0 & \cos\alpha & \sin\alpha \\ 0 & 0 & 0 & 0 & -\sin\alpha & \cos\alpha \end{bmatrix} \quad (6)$$

The correct combined transformation depends on the order of rotations and the exact definition of the coordinate systems see **Erreur ! Source du renvoi introuvable.**. The strains $\varepsilon'' = T_\alpha \varepsilon'$ and $\varepsilon' = T_\theta \varepsilon$, then $\varepsilon'' = T_\alpha T_\theta \varepsilon$. The global stress–strain relationship $\sigma = D_e \varepsilon$ is obtained from the local law $\sigma'' = D_e \varepsilon''$ via:

$$D_e(\theta_e, \alpha_e) = T_{\alpha_e} T_{\theta_e} D_e {T_{\theta_e}}^T {T_{\alpha_e}}^T \quad (7)$$

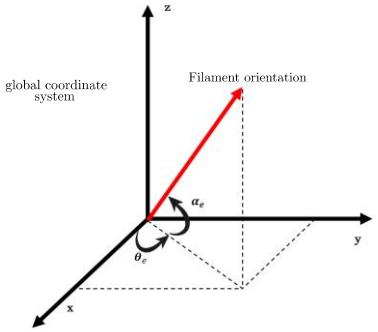


*Figure 3 Three-dimensional coordinate transformation*

The methodology employed in this study is on capturing and simulating the orthotropic elastic behavior resulting from the layer-by-layer deposition process in FDM. Because printing characteristics like layer thickness, raster width, and printing speed have a big effect on the final part's anisotropy, a combined experimental-numerical framework was set up to study these effects. The method uses mechanical testing with multiple loading setups and numerical simulations to find the orthotropic elastic constants that best describe how the material behaves. This iterative approach facilitates the creation of predictive models that connect printing parameters to the actual mechanical performance of the manufactured components. Figure 4 shows how the technique works as a whole. It is set up like this:

- **Selection of FDM printing parameters:** taking into account other AM parameters, such as printing speed, raster width, and infill rate, etc.;

- **Application of a Design of Experiments (DoE):** developing a structured experimental design to examine the impact of the selected parameters;
- **Printing of specimens:** manufacturing standardized specimens in accordance with specific requirements (tensile, shear tests);
- **Conducting mechanical tests:** standardized mechanical tests are used to characterize the mechanical properties of the specimens;
- **Creation of prediction models:** to obtain mathematical models based on the process parameters.

The main goal of this research is to improve the understanding of the influence of printing parameters on the characteristics of parts manufactured by AM, as well as to develop useful methods for anticipating and improving manufacturing processes.

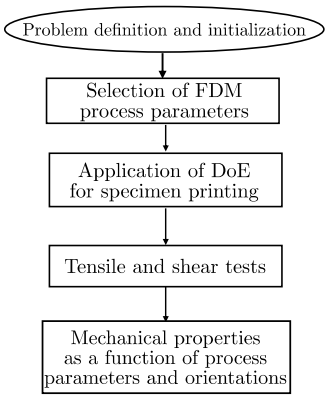


*Figure 4 Methodological flowchart of the experimental approach to develop predictive models*

### 3) Factors of the Design of Experiments

**Parameters influencing mechanical properties**

In this research, the FDM process parameters were selected considering their significant impact on the mechanical characteristics of the produced components, as well as the technical limitations of the equipment used. Their choice was guided by recommendations from the scientific literature and established industrial practices, with the aim of ensuring the quality and reproducibility of the manufactured samples.

According to studies conducted by Phillips[16], various FDM process parameters have a significant influence on the mechanical characteristics of manufactured parts. Taking into account these recommendations as well as the specific constraints of this study, the following parameters were selected:

- **Build orientation:** determines the alignment of the layers relative to the axes of mechanical stress. It directly influences the inter-layer strength and the overall stiffness of the part;
- **Raster width:** raster width affects the printing precision, the flow rate of extruded material, and the thickness of the deposited lines;
- **Layer thickness:** influences the surface quality, precision, and adhesion between layers. An appropriate height helps to limit porosity and ensure better material homogeneity;
- **Number of perimeters:** the peripheral contours reinforce the edges of the part and improve structural cohesion at the periphery;
- Extrusion temperature: controls the fluidity of the extruded material. A good compromise allows for good fusion between layers without degrading the polymer;
- **Printing speed:** affects the manufacturing time and the quality of the deposits. A stable speed contributes to a homogeneous and precise print;
- **Infill pattern and density:** the infill pattern (e.g., rectilinear, hexagonal, or gyroid) determines the internal structure of the part, while the infill density controls the proportion of material deposited inside. These parameters influence the lightness, stiffness, and overall strength of the part.

These choices were made to ensure reliable, reproducible, and well-controlled printing conditions for the subsequent experimental study.

### 4) Parameters selected as factors for the design

In order to propose a new Topology Optimization (TO) method that integrates FDM printing parameters, three main parameters were studied and carefully selected (Layer thickness (t), Raster width (w), and printing speed (S))

## III. Experimental Methodology

### 1) Choice of the Design of Experiments

Designs of experiments are procedures that allow for the optimal organization[17] of experiments conducted within a research method, or particularly in the study of an industrial process or product. The design of experiments can be a tool to model the relationship linking a response $y$ to a set of factors $x_i$.

One should consider designs of experiments if interested in a function of the type:

$$y = f(x_i) \quad (8)$$

With:

*y*: quantity of interest to the experimenter; this quantity is called the response or the quantity of interest;

$x_i$: variables on which the experimenter can act; these variables can be continuous or discontinuous; they are called factors;

*f* : mathematical function that best explains the variations of the response according to the different values given to the $x_i$[18];

It is necessary to list all factors likely to influence the studied phenomenon without excluding any. It has been shown that the number of factors is not a constraint for conducting experiments, and that the use of fractional designs can reduce the number of experiments required. It is necessary to overcome the bad habits acquired through the traditional "one factor at a time" approach and to comprehensively examine all factors likely to influence the responses. It is necessary to abandon dead ends and restrictive assumptions[17].

The selection of one or more responses is of crucial importance. The entire analysis and all conclusions are based on this decision. A response that is inadequate for the problem risks compromising the validity of the experiment or leading to irrelevant conclusions. The chosen response must be clear and unambiguous to accurately answer the question posed. This choice is not as trivial as it might seem, which is sometimes the main obstacle one faces. For example, we have devoted considerable time and exceptional creativity to develop a precise method for measuring the effervescence of mineral water or assessing the stress level of air traffic controllers[17].

When studying a factor $x_i$, such as temperature for example, it is not significantly modified. A lower value and an upper value are always defined according to the requirements of the study. The variations of the factor are thus constrained by two limits. The experimenter retains the lower bound as the "low level" and the upper bound as the "high level". It is common to identify the low level of a factor with a minus sign (-) and its high level with a plus sign (+)[18].

Designs of experiments allow obtaining a maximum of information by carrying out a minimum number of tests. For this, it is necessary to know the basic mathematical principles to use them well and to adopt a methodical approach[18].

The selected printing parameters were defined based on material supplier recommendations and commonly adopted values reported in the literature for FDM-processed PLA. An extrusion temperature of 200 °C was chosen to ensure sufficient melt flow and interlayer bonding without inducing thermal degradation. A build plate temperature of 60 °C, close to the glass transition temperature of PLA, was adopted to improve first-layer adhesion and reduce warping. These conditions represent a well-established compromise between print quality, dimensional stability, and mechanical performance in standard FDM environments.

**Presentation of the Box-Behnken Design**

The experimental approach derived from Box-Behnken is crucial for the study of complex phenomena affected by several quantitative factors, thus allowing for an optimal exploration of the main effects and interactions between variables.

The experimental design was developed to establish several levels of study in order to evaluate quadratic effects and to integrate central points to adjust the variance and serve the model, which makes it a tool for supporting non-linearities and interactions between variables[19].

In this work, we discuss the factors affecting the mechanical performance of printed parts such as layer thickness, raster width (nozzle diameter), and printing speed. Tests were organized according to a DoE with three levels for each parameter, making the tests precise and reliable. For each factor, a DoE was carried out and allowed for interaction studies and the highlighting of non-linear effects. Finally, in order to better model the phenomena influencing the test results and to be able to accurately predict the performance of the manufactured parts, intermediate tests were added.

The following Table 1 presents the studied factors as well as the levels chosen for each:

*Table 1 Levels of the parameters for the design of experiments*

| Parameter | Symbol | Level 1 | Level 2 | Level 3 |
|---|---|---|---|---|
| Width (mm) | w | 0.3 | 0.4 | 0.5 |
| Speed (mm/s) | S | 50 | 65 | 80 |
| Thickness (mm) | t | 0.08 | 0.14 | 0.20 |

**2) Design Construction**

The Box-Behnken method was used with Minitab software to organize the experimental tests. This experimental design was chosen for its ability to model quadratic effects while reducing the total number of required tests.

The Box-Behnken design produced 13 combinations of tests, considering the three study factors (layer thickness, raster width (nozzle diameter), and printing speed), each at three

levels. While maximizing experimental resources, this method allows for a rapid examination of the individual influence of the parameters as well as their interactions.

The following Table 2 illustrates the combinations obtained for the different tests:

*Table 2 Table of test parameters*

| Order | w (mm) | T (mm) | S (mm/s) |
|---|---|---|---|
| 1 | 0.3 | 0.08 | 65 |
| 2 | 0.5 | 0.08 | 65 |
| 3 | 0.3 | 0.20 | 65 |
| 4 | 0.5 | 0.20 | 65 |
| 5 | 0.3 | 0.14 | 50 |
| 6 | 0.5 | 0.14 | 50 |
| 7 | 0.3 | 0.14 | 80 |
| 8 | 0.5 | 0.14 | 80 |
| 9 | 0.4 | 0.08 | 50 |
| 10 | 0.4 | 0.20 | 50 |
| 11 | 0.4 | 0.08 | 80 |
| 12 | 0.4 | 0.20 | 80 |
| 13 | 0.4 | 0.14 | 65 |

### 3) Printing of the Samples

#### a) Description of Specimen Standards

To comprehensively evaluate the influence of printing parameters on mechanical properties, each combination from the Box-Behnken design of experiments was used to manufacture two types of specimens:

- **Specimens for tensile tests**
  The tensile tests will be carried out in accordance with the **ISO 527-2** standard[20]. Although this standard was initially developed for conventional polymers, it is perfectly applicable to materials manufactured by FDM 3D printing. In the absence of a specific standard dedicated to printed parts, the use of ISO 527-2 remains justified, as confirmed by the study of Spoerk et al[16]. The dimensions of the type 1BA specimen, specifically dedicated to tensile tests according to this standard, are illustrated in detail in Figure 5.

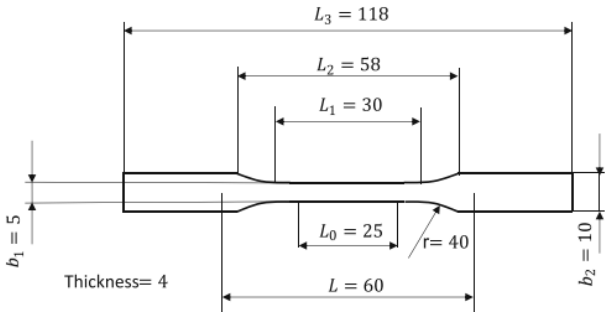


*Figure 5 Specimen according to ISO 527-2 type 1BA "tensile strength" test sample (dimensions in mm)*

- **specimens for shear tests**
  For this test, a cylindrical specimen with a **diameter** of 6 mm and a **length** of 60 mm was used. Its geometry is inspired by the **ASTM E8 – Method C** standard, which defines the standard dimensions of specimens for tensile tests, even for a shear test protocol.

#### b) Experimental Conditions for Printing

To account for the effect of the build orientation, each model was printed in three main directions, printing along the *X'*-axis, *Y'*-axis, and *Z'*-axis.

The mechanical specimens were produced by FDM using a Creality Ender 3-V2 printer (Figure 6) and PLA (polylactic acid) filament.

*Figure 6 Creality Ender 3-V2*

Several printing parameters were intentionally maintained constant throughout the manufacturing process to ensure experimental reproducibility. These parameters were chosen to ensure optimal print quality while minimizing sources of variability:

- Material: PLA (diameter 1.75 mm). PLA is a thermoplastic polymer widely used in 3D printing for its good mechanical properties;
- Extrusion temperature: 200\degree C. This temperature is in the optimal range recommended for PLA;
- Bed temperature: 60\degree C. Maintaining this temperature improves the adhesion of the first layer to the bed, thus reducing the risk of detachment or warping;
- Infill density: 100\%. A full infill was chosen to simulate a nearly dense and homogeneous material to minimize internal voids. This allows obtaining mechanical results representative of the solid material and limiting the influence of porosity on the measured properties;
- Infill pattern: rectilinear. The rectilinear pattern promotes a uniform distribution of mechanical loads during tests, while facilitating control of the printing path;
- Number of perimeters: 1 perimeter. A single peripheral contour was defined to ensure continuity with the infill area and to maintain the nominal dimensions of the specimens.

All prints were made from standardized digital models exported in STL format, then sliced using dedicated software respecting the mentioned parameters. To preserve the integrity of the parts printed directly to the final size, no machining or post-processing operations were performed.

Each specimen was rigorously identified and stored to ensure proper tracking during the mechanical testing campaigns.

The printing of specimens is shown in Figure 7.

*Figure 7 Printing of a specimen along the Z-axis*

**4) Tensile Tests**

The tensile tests were carried out in accordance with the ISO 527-2 standard. Figure 8(a), (b) and (c) show printing along the *X'*-axis, *Y*'-axis and *Z'*-axis respectively.

$(a)$ $(b)$ $(c)$

*Figure 8 Tensile test specimens*

**c) Equipment and Test Conditions**

The tests were carried out using a MTS universal testing machine Figure 9, equipped with a 10 KN load cell suitable for the low stresses characteristic of polymer materials.

*Figure 9 Tensile test*

The main test conditions are:

- Specimen shape}: see Figure 5 ISO 527-2;
- Test speed: 0.25 mm/min according to ISO 527-1;
- Area for Young's modulus calculation: defined between 0.05\% and 0.25\% of deformation.

**5) Shear Tests**

The shear tests were carried out according to an adapted protocol based on the principles of the ASTM E8 standard (Method C)[21].

Although this standard was originally intended for tensile testing of metallic materials, its methodology was adapted here for the evaluation of the shear behavior of printed polymer materials. Figure 10 show printing along the *X'*-axis, *Y*'-axis and *Z'*-axis respectively

*Figure 10 Shear test specimens*

The tests were performed on the MTS universal testing machine (Figure 11), using a specific clamping device to apply a pure shear force.

*Figure 11 Shear test*

The main test conditions are as follows:

- Specimen shape: specimens adapted for shear tests, inspired by the geometric specifications recommended for simple shear type tests;
- Dimensions: diameter 6 mm and total length 60 mm;
- Test speed: 1 mm/min, a rate used for tensile tests to ensure consistent comparison.

## IV. Results & Discussion

### 1) Presentation of Raw Data

The material characterization step involved exhaustive mechanical testing campaigns, specifically tensile and shear tests. These tests were conducted on meticulously 3D printed (FDM) specimens, whose manufacturing followed a rigorous Box-Behnken design of experiments.

This design allowed for the systematic exploration of the influence of three key printing parameters (w, t, and S) on the intrinsic elastic properties of the material. Table 3 and Table 4, presented below, record all the raw results from these investigations.

They detail, for each unique combination of tested printing parameters, the measured values of the longitudinal and transverse Young's moduli ($E_{X'}$, $E_{Y'}$, $E_{Z'}$) as well as the corresponding shear moduli ($G_{X'Y'}$, $G_{Y'Z'}$, $G_{X'Z'}$). This primary data, obtained experimentally, constitutes the essential foundation on which subsequent statistical analyses and, ultimately, the construction of predictive models will be based.

*Table 3 Experimental results for Young's moduli*

| w (mm) | t (mm) | S (mm/s) | $E_{X'}$ (GPa) | $E_{Y'}$ (GPa) | $E_{Z'}$ (GPa) |
|---|---|---|---|---|---|
| 0.3 | 0.08 | 65 | 1.57200 | 1.27150 | 0.98910 |
| 0.5 | 0.08 | 65 | 1.53930 | 1.20280 | 0.90009 |
| 0.3 | 0.20 | 65 | 1.53080 | 1.10270 | 0.86710 |
| 0.5 | 0.20 | 65 | 1.26180 | 1.03190 | 0.74084 |
| 0.3 | 0.14 | 50 | 1.50460 | 1.26660 | 0.95280 |
| 0.5 | 0.14 | 50 | 1.32549 | 1.08628 | 0.81850 |
| 0.3 | 0.14 | 80 | 1.50820 | 1.25501 | 0.92980 |
| 0.5 | 0.14 | 80 | 1.14060 | 1.04730 | 0.82433 |
| 0.4 | 0.08 | 50 | 1.40030 | 1.21030 | 0.89238 |
| 0.4 | 0.20 | 50 | 1.31250 | 1.14130 | 0.87275 |
| 0.4 | 0.08 | 80 | 1.22900 | 1.04700 | 0.79224 |
| 0.4 | 0.20 | 80 | 1.11550 | 0.98540 | 0.74462 |
| 0.4 | 0.14 | 65 | 1.33040 | 1.13490 | 0.81552 |

*Table 4 Experimental results for shear moduli*

| w (mm) | t (mm) | S (mm/s) | $E_{X'}$ (GPa) | $E_{Y'}$ (GPa) | $E_{Z'}$ (GPa) |
|---|---|---|---|---|---|
| 0.3 | 0.08 | 65 | 0.77460 | 0.66575 | 0.79560 |
| 0.5 | 0.08 | 65 | 0.69190 | 0.49595 | 0.58755 |
| 0.3 | 0.20 | 65 | 0.73535 | 0.48285 | 0.60425 |
| 0.5 | 0.20 | 65 | 0.56985 | 0.46985 | 0.58895 |
| 0.3 | 0.14 | 50 | 0.71110 | 0.67450 | 0.76325 |
| 0.5 | 0.14 | 50 | 0.52415 | 0.64145 | 0.69215 |
| 0.3 | 0.14 | 80 | 0.68925 | 0.58080 | 0.65870 |
| 0.5 | 0.14 | 80 | 0.47385 | 0.52190 | 0.52190 |
| 0.4 | 0.08 | 50 | 0.60585 | 0.69860 | 0.77530 |
| 0.4 | 0.20 | 50 | 0.63910 | 0.63530 | 0.70610 |
| 0.4 | 0.08 | 80 | 0.58185 | 0.63675 | 0.72805 |
| 0.4 | 0.20 | 80 | 0.30995 | 0.37650 | 0.50860 |
| 0.4 | 0.14 | 65 | 0.55980 | 0.42930 | 0.69095 |

### 2) Stress-Strain Curves (Tensile + Shear)

To thoroughly analyze and visually interpret the complex effects of printing parameters on the mechanical properties of FDM-manufactured parts, several types of graphical representations were used. These visual tools are essential for understanding not only the overall behavior of the material but also the nuances induced by variations in manufacturing conditions.

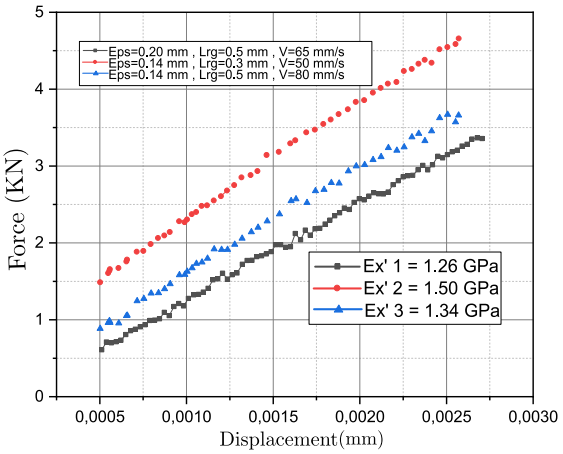


*Figure 12 Force–displacement curves and elastic moduli: Effect of process parameters on EX'*

Data from tensile tests systematically conducted along the three orthogonal axes (*X'*, *Y'*, and *Z'*) were utilized. These tests are fundamental because they allow for a detailed examination of the influence of key printing factors—such as raster width, layer thickness, and printing speed—on the directional mechanical characteristics of 3D components. The raw force-displacement curves, recorded during each tensile test, are the primary source of information for evaluating the Young's modulus under various parameters.

The results demonstrate a significant influence of printing orientation on the elastic stiffness of the material. Reflecting good mechanical behavior, the moduli in the X'-direction, shown in Figure 12, range from 1.26 to 1.50 GPa.

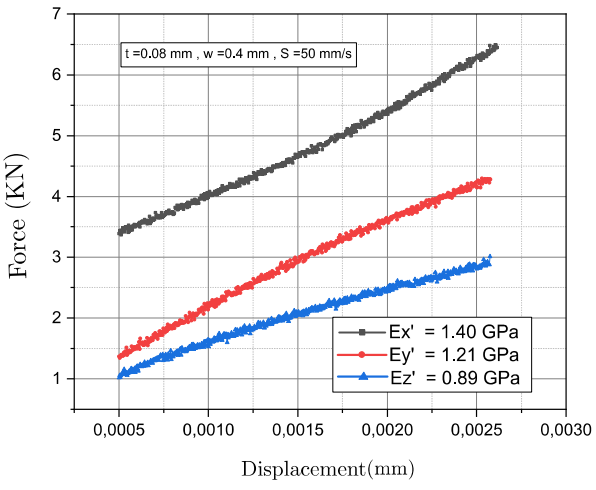


*Figure 13 Force–displacement curves and elastic moduli: Comparison of orthotropic moduli for a fixed parameter set*

A comparison with constant parameters, shown in Figure 13, confirms the orthotropic behavior of the material: stiffness is maximal in X', intermediate in Y', and minimal in Z'.

Ultimately, the mechanical behavior of FDM components is strongly influenced by the printing direction and associated parameters; the process's anisotropy must be taken into account in the design.

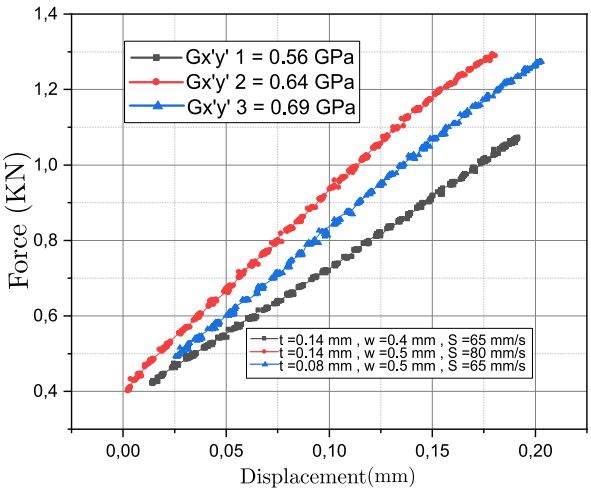


*Figure 14 Force-displacement curves and shear moduli: Parameter effect on GX'Y'*

Figure 14shows the shear response in the *X'Y'* plane for three printing configurations. The obtained moduli vary from 0.56 GPa to 0.69 GPa, demonstrating a marked sensitivity to manufacturing parameters.

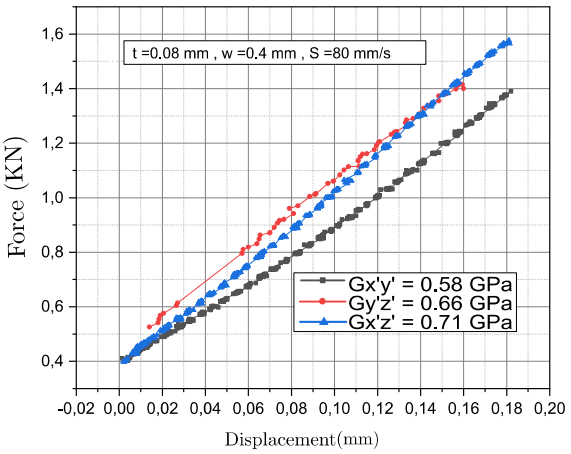


*Figure 15 Force-displacement curves and shear moduli: Comparison of orthotropic shear moduli for a fixed parameter set*

Figure 15 summarizes the results by directly comparing the three shear moduli for the same set of printing parameters. Anisotropy is clearly visible: $G_{X'Z'}$ = 0.71 GPa is the highest, followed by $G_{Y'Z'}$ = 0.66$ GPa, then $G_{X'Y'}$ = 0.58 GPa.

Overall, these experimental results clearly highlight the pronounced anisotropic behavior of FDM-manufactured PLA in shear, strongly influenced by the loading direction and by

printing parameters, especially the orientation of intra-layer deposition.

In the linear elastic regime, force–displacement measurements can be directly used to derive stress–strain responses through standard mechanical relationships. Specifically, the applied force is converted into stress using the nominal cross-sectional area, while the measured displacement is converted into strain using the initial gauge length of the specimen.

Since all tests were conducted within the elastic domain and under controlled boundary conditions, the resulting stress–strain curves are mechanically equivalent representations of the experimentally recorded force–displacement data. This approach is commonly adopted in experimental mechanics and does not affect the validity of the extracted elastic moduli.

The corresponding stress and strain values were calculated as follows:

**Axial tests (Young's modulus):**

$$\sigma = \frac{F}{A} \quad , \qquad \varepsilon = \frac{\Delta L}{L_0} \tag{9}$$

where:

- $\sigma$ : axial stress (Pa)
- $\varepsilon$ : axial strain (dimensionless)
- F : applied force (N)
- A : cross-sectional area of the specimen (m²)
- ΔL : measured elongation (m)
- $L_0$ : initial length of the specimen (m)

**Shear tests (Shear modulus):**

$$\tau = \frac{F}{2A} \quad , \qquad \gamma = \frac{\Delta D}{D_0} \tag{10}$$

where:

- $\tau$ : shear stress (Pa)
- $\gamma$ : shear strain (dimensionless)
- F = applied shear force (N)
- A = shear area ($A = \pi \frac{D^2}{4}$) of the specimen (m²)
- ΔD = measured shear displacement (m)
- $D_0$ = initial diameter in shear (m)

The Young's modulus E and the shear modulus G were then obtained from the slope of the linear region of the stress-strain curves:

$$E = \frac{\sigma}{\varepsilon} \quad , \qquad E = \frac{\tau}{\gamma} \tag{11}$$

### 3) Predictive Models for Elastic Moduli

Quadratic polynomial models were established from the experimental results and the statistical analysis of the design of experiments to estimate the elastic moduli ($E_{X'}$, $E_{Y'}$, $E_{Z'}$) and shear moduli ($G_{X'Y'}$, $G_{Y'Z'}$, $G_{X'Z'}$) as a function of three printing parameters (w (mm), t (mm), and S (mm/s)).

The analysis of variance (ANOVA) allows for the evaluation of the influence of these parameters on the mechanical properties of the printed parts, by identifying the significant effects of the factors and their interactions.

#### a) Model for Young's Modulus $E_{X'}$

The analysis of variance (ANOVA) Table 5 indicates that the prediction model for the Young's modulus $E_{X'}$ is globally significant, with a p-value of 0.006 for the entire model. This means that the considered factors reliably explain the variation in the mechanical response.

Therefore, raster width is the dominant factor in the variation of $E_{X'}$, followed by layer thickness and printing speed. The quadratic effects and interactions enhance the quality of the model, although their contribution varies in different cases.

*Table 5 Analysis of Variance Table for EX'*

| Source | DF | Adj SS | Adj MS | F-Value | p-Value |
|---|---|---|---|---|---|
| Model | 7 | 0.274490 | 0.039213 | 13.35 | 0.006 |
| Linear | 3 | 0.161531 | 0.053844 | 18.33 | 0.004 |
| w | 1 | 0.089975 | 0.089975 | 30.63 | 0.003 |
| t | 1 | 0.033800 | 0.033800 | 11.51 | 0.019 |
| S | 1 | 0.037756 | 0.037756 | 12.85 | 0.016 |
| Square | 2 | 0.090118 | 0.045059 | 15.34 | 0.007 |
| $w^2$ | 1 | 0.038249 | 0.038249 | 13.02 | 0.015 |
| $S^2$ | 1 | 0.025149 | 0.025149 | 8.56 | 0.033 |
| Interaction | 2 | 0.022842 | 0.011421 | 3.89 | 0.096 |
| w.t | 1 | 0.013959 | 0.013959 | 4.75 | 0.081 |
| w.S | 1 | 0.008882 | 0.008882 | 3.02 | 0.143 |
| Error | 5 | 0.014686 | 0.002937 | | |
| Total | 12 | 0.289176 | | | |

The resulting equation for $E_{X'}$ is as follows (results are given in GPa):

$$E_{X'} = 0.95 - 6.99w + 2.85\,t + 0.0627\,S + 11.69\,w^2 - 0.000421\,S^2 - 9.85\,w.t - 0.0314\,w.S \tag{12}$$

### b) Model for Young's Modulus $E_{Y'}$

The ANOVA Table 6 shows that the prediction model for the transverse Young's modulus $E_{Y'}$ is globally significant, with a p-value of 0.008 for the complete model. This indicates that the studied parameters satisfactorily explain the variation in the mechanical response $E_{Y'}$.

*Table 6 Analysis of Variance Table for EY'*

| Source | DF | Adj SS | Adj MS | F-Value | p-Value |
|---|---|---|---|---|---|
| Model | 4 | 0.088574 | 0.022144 | 7.42 | 0.008 |
| Linear | 3 | 0.079525 | 0.026508 | 8.88 | 0.006 |
| w | 1 | 0.034786 | 0.034786 | 11.65 | 0.009 |
| t | 1 | 0.027648 | 0.027648 | 9.26 | 0.016 |
| S | 1 | 0.017091 | 0.017091 | 5.72 | 0.044 |
| Square | 1 | 0.009049 | 0.009049 | 3.03 | 0.120 |
| $w^2$ | 1 | 0.009049 | 0.009049 | 3.03 | 0.120 |
| Error | 8 | 0.023887 | 0.002986 | | |
| Total | 12 | 0.112462 | | | |

The resulting equation for $E_{Y'}$ is as follows (results are given in GPa):

$$E_{Y'} = 2.573 - 5\,w + 0.98\,t + 0.00308\,S + 5.42\,w^2 \quad (13)$$

### c) Model for Young's Modulus $E_{Z'}$

The analysis of variance for the prediction model of $E_{Z'}$ Table 7 (vertical Young's modulus) indicates that the model is globally significant, with a p-value of 0.004. This confirms that the selected input variables satisfactorily explain the variation in the response.

*Table 7 Analysis of Variance Table for EZ'*

| Source | DF | Adj SS | Adj MS | F-Value | tp-Value |
|---|---|---|---|---|---|
| Model | 4 | 0.057671 | 0.014418 | 9.38 | t0.004 |
| Linear | 3 | 0.048593 | 0.016198 | 10.54 | t0.004 |
| w | 1 | 0.025882 | 0.025882 | 16.83 | t0.003 |
| t | 1 | 0.015181 | 0.015181 | 9.87 | t0.014 |
| S | 1 | 0.007530 | 0.007530 | 4.90 | t0.058 |
| Square | 1 | 0.009078 | 0.009078 | 5.90 | t0.041 |
| $w^2$ | 1 | 0.009078 | 0.009078 | 5.90 | t0.041 |
| Error | 8 | 0.012300 | 0.001537 | | |
| Total | 12 | 0.069970 | | | |

The resulting equation for $E_{Z'}$ is as follows (results are given in GPa):

$$E_{Z'} = 2.155 - 4.91\,w - 0.726\,t - 0.002045\,S + 5.43\,w^2 \quad (14)$$

### d) Model for Shear Modulus $G_{X'Y'}$

The prediction model for modulus $G_{X'Y'}$ is globally significant (shown in ANOVA Table 8 ) (F = 9.34, p = 0.008), confirming that the studied parameters satisfactorily explain the variation of $G_{X'Y'}$.

*Table 8 Analysis of Variance Table for GX'Y'*

| Source | DF | Adj SS | Adj MS | F-Value | p-Value |
|---|---|---|---|---|---|
| Model | 6 | 0.16931 | 0.028218 | 9.34 | 0.008 |
| Linear | 3 | 0.09551 | 0.031836 | 10.54 | 0.008 |
| w | 1 | 0.05290 | 0.052902 | 17.51 | 0.006 |
| t | 1 | 0.02000 | 0.019995 | 6.62 | 0.042 |
| S | 1 | 0.02261 | 0.022610 | 7.48 | 0.034 |
| Square | 2 | 0.05052 | 0.025260 | 8.36 | 0.018 |
| $w^2$ | 1 | 0.02011 | 0.020111 | 6.66 | 0.042 |
| $S^2$ | 1 | 0.01533 | 0.015328 | 5.07 | 0.065 |
| Interaction | 1 | 0.02328 | 0.023279 | 7.71 | 0.032 |
| t.S | 1 | 0.02328 | 0.023279 | 7.71 | 0.032 |
| Error | 6 | 0.01813 | 0.003021 | | |
| Total | 12 | 0.18743 | | | |

The resulting equation for $G_{X'Y'}$ is as follows (results are given in GPa):

$$G_{X'Y'} = 0.466 - 7.59\,w + 0.4.68\,t + 0.0511\,S + 8.47\,w^2\ 0.000329\,S^2 - 0.0848\,t.S \quad (15)$$

### e) Model for Shear Modulus $G_{Y'Z'}$

The prediction model for modulus $G_{Y'Z'}$ is highly significant (shown in ANOVA Table 9) (F = 14.97, p = 0.010), demonstrating an excellent fit to the experimental data.

*Table 9 Analysis of Variance Table for GY'Z'*

| Source | DF | Adj SS | Adj MS | F-Value | p-Value |
|---|---|---|---|---|---|
| Model | 8 | 0.128171 | 0.016021 | 14.97 | 0.010 |
| Linear | 3 | 0.080518 | 0.026839 | 25.08 | 0.005 |
| w | 1 | 0.009436 | 0.009436 | 8.82 | 0.041 |
| t | 1 | 0.035451 | 0.035451 | 33.13 | 0.005 |
| S | 1 | 0.035631 | 0.035631 | 33.29 | 0.004 |
| Square | 3 | 0.031809 | 0.010603 | 9.91 | 0.025 |
| $w^2$ | 1 | 0.007846 | 0.007846 | 7.33 | 0.054 |
| $t^2$ | 1 | 0.003789 | 0.003789 | 3.54 | 0.133 |
| $S^2$ | 1 | 0.031169 | 0.031169 | 29.12 | 0.006 |
| Interaction | 2 | 0.015844 | 0.007922 | 7.40 | 0.045 |
| w.t | 1 | 0.006147 | 0.006147 | 5.74 | 0.075 |
| t.S | 1 | 0.009697 | 0.009697 | 9.06 | 0.040 |
| Error | 4 | 0.004281 | 0.001070 | | |
| Total | 12 | 0.132452 | | | |

The resulting equation for $G_{Y'Z'}$ is as follows (results are given in GPa):

$$G_{Y'Z'} = 4.231 - 5.95\,w + 3.33\,t - 0.0643\,S + 5.86\,w^2 + 11.31\,t^2 + 0.000519\,S^2 + 6.53\,w.t - 0.0547\,t.S \quad (16)$$

### f) Model for Shear Modulus $G_{X'Z'}$

The prediction model for modulus $G_{X'Z'}$ is highly significant (shown in ANOVA Table 10) (F = 11.31, p = 0.003), explaining 89.0% of the total variance ($R^2$= 0.076623/0.086110).

The resulting equation for $G_{X'Z'}$ is as follows (results are given in GPa):

$$G_{X'Z'} = 1.259 - 1.52\,w - 1.5\,t + 0.00247\,S + 8.03\,w.t - 0.0417\,t.S \quad (17)$$

*Table 10 Analysis of Variance Table for GX'Z'*

| Source | DF | Adj SS | Adj MS | F-Value | p-Value |
|---|---|---|---|---|---|
| Model | 5 | 0.076623 | 0.015325 | 11.31 | 0.003 |
| Linear | 3 | 0.061691 | 0.020564 | 15.17 | 0.002 |
| w | 1 | 0.012545 | 0.012545 | 9.26 | 0.019 |
| t | 1 | 0.028632 | 0.028632 | 21.12 | 0.002 |
| speed | 1 | 0.020513 | 0.020513 | 15.13 | 0.006 |
| Interaction | 2 | 0.014932 | 0.007466 | 5.51 | 0.037 |
| w.t | 1 | 0.009288 | 0.009288 | 6.85 | 0.035 |
| t.S | 1 | 0.005644 | 0.005644 | 4.16 | 0.081 |
| Error | 7 | 0.009488 | 0.001355 | | |
| Total | 12 | 0.086110 | | | |

The robustness of the proposed regression models was evaluated using the coefficient of determination ($R^2$). High $R^2$ values were obtained for all predicted elastic properties, indicating strong agreement between experimental results and model predictions. The remaining discrepancies are primarily attributed to the intrinsic variability of the FDM process. Overall, the models provide reliable predictive capability within the investigated parameter space.

## V. Conclusion

This study developed a comprehensive methodology to predict the mechanical properties of FDM printed parts. Through a Box-Behnken design of experiments, we analyzed the impact of three key parameters: raster width, layer thickness, and printing speed.

The results reveal a marked anisotropy, with longitudinal moduli ($E_{X'}$) significantly higher than transverse moduli ($E_{Z'}$), due to the limitations of interlayer adhesion. Statistical analysis allowed for the establishment of predictive models highlighting complex relationships including non-linear effects and interactions between parameters.

The generated response surfaces identify optimal combinations of parameters, offering valuable tools for optimization. These models, statistically significant ($p<0.05$) and predictive ($R^2>89\%$), open up prospects for integration into topology optimization algorithms.

In conclusion, this research provides both a fundamental understanding of the parameter-property relationships and practical tools for optimizing printed parts, while emphasizing the crucial importance of considering the inherent anisotropy of the FDM process.

Future work can further develop these methods to optimize the performance of 3D-printed materials, making AM a crucial element of contemporary engineering. Additionally, TO optimization, in conjunction with PSP relationships, can address other design constraints, such as stress and overhanging features.

***References:***

**1.** B. Sanderson, F. Diba, H. Kishawy, et A. Hosseini, « Finite element analysis of additive manufacturing of polymers using selective laser sintering », *Int. J. Adv. Manuf. Technol.*, vol. 129, nº 3-4, p. 1631-1647, nov. 2023, doi: 10.1007/s00170-023-12370-5.

**2.** M. Daly, M. Tarfaoui, M. Chihi, et C. Bouraoui, « FDM technology and the effect of printing parameters on the tensile strength of ABS parts », *Int. J. Adv. Manuf. Technol.*, vol. 126, nº 11-12, p. 5307-5323, juin 2023, doi: 10.1007/s00170-023-11486-y.

**3.** A. Bellini et S. Güçeri, « Mechanical characterization of parts fabricated using fused deposition modeling », *Rapid Prototyp. J.*, vol. 9, nº 4, p. 252-264, 2003.

**4.** Z. H. U. Jihong, Z. Han, W. Chuang, Z. Lu, et Y. Shangqin, « A review of topology optimization for additive manufacturing: Status and challenges », *Chin. J. Aeronaut.*, vol. 34, nº 1, p. 91-110, 2021.

**5.** S. Xu, J. Huang, J. Liu, et Y. Ma, « Topology optimization for FDM parts considering the hybrid deposition path pattern », *Micromachines*, vol. 11, nº 8, p. 709, 2020.

**6.** J. Zou et X. Xia, « Topology optimization for additive manufacturing with strength constraints considering anisotropy », *J. Comput. Des. Eng.*, vol. 10, nº 2, p. 892-904, 2023.

**7.** Y. Zhou, T. Nomura, et K. Saitou, « Anisotropic multicomponent topology optimization for additive manufacturing with build orientation design and stress-constrained interfaces », *J. Comput. Inf. Sci. Eng.*, vol. 21, nº 1, p. 011007, 2021.

**8.** J.-H. Zhu, W.-H. Zhang, et L. Xia, « Topology Optimization in Aircraft and Aerospace Structures

Design », *Arch. Comput. Methods Eng.*, vol. 23, nº 4, p. 595-622, déc. 2016, doi: 10.1007/s11831-015-9151-2.

**9.** J. Plocher et A. Panesar, « Review on design and structural optimisation in additive manufacturing: Towards next-generation lightweight structures », *Mater. Des.*, vol. 183, p. 108164, 2019.

**10.** J. Liu *et al.*, « Current and future trends in topology optimization for additive manufacturing », *Struct. Multidiscip. Optim.*, vol. 57, nº 6, p. 2457-2483, juin 2018, doi: 10.1007/s00158-018-1994-3.

**11.** G. Allaire, C. Dapogny, R. Estevez, A. Faure, et G. Michailidis, « Structural optimization under overhang constraints imposed by additive manufacturing technologies », *J. Comput. Phys.*, vol. 351, p. 295-328, 2017.

**12.** L. Cheng, J. Liu, X. Liang, et A. C. To, « Coupling lattice structure topology optimization with design-dependent feature evolution for additive manufactured heat conduction design », *Comput. Methods Appl. Mech. Eng.*, vol. 332, p. 408-439, 2018.

**13.** Y. Mehir, A. Benaouali, et Y. Benabid, « Integration of FDM process-structure relationship in topology optimization formulation », *Int. J. Adv. Manuf. Technol.*, vol. 136, nº 3-4, p. 1483-1499, janv. 2025, doi: 10.1007/s00170-024-14929-2.

**14.** E. J. Barbero, *Introduction to composite materials design*. CRC press, 2010. Consulté le: 26 octobre 2025. [En ligne]. Disponible sur: https://www.taylorfrancis.com/books/mono/10.1201/9781439894132/introduction-composite-materials-design-ever-barbero

**15.** D. Jiang, « Three dimensional topology optimization with orthotropic material orientation design for additive manufacturing structures. », PhD Thesis, 2017. Consulté le: 16 décembre 2025. [En ligne]. Disponible sur: https://baylor-ir.tdl.org/items/a519894b-d709-4d20-9376-7a744237f67c

**16.** C. Phillips, M. Kortschot, et F. Azhari, « Towards standardizing the preparation of test specimens made with material extrusion: Review of current techniques for tensile testing », *Addit. Manuf.*, vol. 58, p. 103050, 2022.

**17.** J. Goupy et L. Creighton, *Introduction aux plans d'expériences-3ème édition-Livre+ CD-Rom*. Hachette, 2006.

**18.** B. ATSAMENIA, « Etude de l'effet des paramètres de synthèse sur les propriétés des dépôts de Nickel en utilisant la méthode des plans d'expériences », 2019, Consulté le: 26 octobre 2025. [En ligne]. Disponible sur: https://dspace.univ-guelma.dz/jspui/handle/123456789/4141

**19.** G. E. P. Box et D. W. Behnken, « Some New Three Level Designs for the Study of Quantitative Variables », *Technometrics*, vol. 2, nº 4, p. 455-475, nov. 1960, doi: 10.1080/00401706.1960.10489912.

**20.** G. CCS, « Plastics–determination of tensile properties–part 2: test conditions for moulding and extrusion plastics », 2013, Consulté le: 26 octobre 2025. [En ligne]. Disponible sur: https://www.chinesestandard.net/PDF-EN/GBT1040.2-2022EN-P07P-H5544H-436703.pdf

**21.** I. Astm, « ASTM E8/E8M-16a: standard test methods for tension testing of metallic materials », *West Conshohocken PA USA ASTM Int.*, 2016.